

RESEARCH ARTICLE

10.1029/2020JD033720

Special Section:

Southern Ocean clouds,
aerosols, precipitation and
radiation

Key Points:

- The dispersion of cloud droplet size distributions (ϵ) increases with increasing aerosol loading for a limited range of vertical velocity (w)
- The ϵ decreases with increasing w for a limited range of low-level aerosol loading
- The ϵ decreases with height rapidly from cloud base (0.42 ± 0.13) and then remains relatively constant in the upper cloud layer (0.27 ± 0.09)

Supporting Information:

- Supporting Information S1

Correspondence to:

C. Zhao,
czhao@bnu.edu.cn

Citation:

Wang, Y., Zhao, C., McFarquhar, G. M., Wu, W., Reeves, M., & Li, J. (2021). Dispersion of droplet size distributions in supercooled non-precipitating stratocumulus from aircraft observations obtained during the Southern Ocean Cloud Radiation Aerosol Transport Experimental Study. *Journal of Geophysical Research: Atmospheres*, 126, e2020JD033720. <https://doi.org/10.1029/2020JD033720>

Received 18 AUG 2020

Accepted 23 FEB 2021

© 2021. American Geophysical Union.
All Rights Reserved.

Dispersion of Droplet Size Distributions in Supercooled Non-precipitating Stratocumulus from Aircraft Observations Obtained during the Southern Ocean Cloud Radiation Aerosol Transport Experimental Study

Yang Wang^{1,2,3} , Chuanfeng Zhao² , Greg M. McFarquhar^{3,4} , Wei Wu³ , Mike Reeves⁵, and Jiming Li¹ 

¹College of Atmospheric Sciences, Lanzhou University, Lanzhou, China, ²College of Global Change and Earth System Science, State Key Laboratory of Earth Surface Processes and Resource Ecology, Beijing Normal University, Beijing, China, ³Cooperative Institute for Mesoscale Meteorological Studies, University of Oklahoma, Norman, OK, USA, ⁴School of Meteorology, University of Oklahoma, Norman, OK, USA, ⁵National Center for Atmospheric Research, Boulder, CO, USA

Abstract The characteristics of cloud droplet size distributions and statistical relations of the relative dispersion (ϵ) with the vertical velocity (w) and with the interstitial aerosol concentration (N_{ia}) are investigated for ubiquitous supercooled shallow stratocumulus observed over the Southern Ocean (SO) using aircraft measurements obtained during the Southern Ocean Cloud Radiation Aerosol Transport Experimental Study. Distinct vertical variations have been found using 36 non-precipitating cloud profiles. The cloud droplet effective radius (r_e) increases nearly monotonically from $5.3 \pm 1.9 \mu\text{m}$ at cloud base to $9.4 \pm 2.2 \mu\text{m}$ at cloud top. The ϵ decreases rapidly from cloud base (0.42 ± 0.13) and then remains relatively constant in the upper cloud layer (0.27 ± 0.09). This study also shows robust dependence of ϵ on both N_{ia} and w . The ϵ increases (decreases) with increasing N_{ia} (w) at a 95% confidence level when values of w (low N_{ia}) are restricted to a small range. The important roles of aerosols and dynamics on ϵ are demonstrated and are crucial to estimating aerosol indirect radiative forcing, especially for pristine SO regions where models almost universally underestimate reflected radiation.

Plain Language Summary For numerical studies of aerosol cloud interactions, parameterizations are not always well suited because the basis of the relationship between the droplet concentration (modified by aerosols and cloud dynamics) and cloud radiative properties cannot be easily observed and characterized due to many interfering effects such as the cloud droplet activation process, mixing, entrainment, and drizzle scavenging. In this study, droplet size distributions (DSDs) are characterized and their relations to interstitial aerosol concentration (N_{ia}) and vertical velocity (w) are isolated using in situ aircraft observations for shallow stratocumulus over the pristine Southern Ocean (SO). The relative dispersion (ϵ) increases (decreases) with increasing N_{ia} (w) when nearly excluding the cloud dynamic (aerosol loading) effect. This work will be particularly useful in the development of robust parameterizations of DSD properties and their interaction with aerosols for shallow ice-free clouds over the SO.

1. Introduction

The shape of cloud droplet size distributions (DSDs), the effective radius (r_e), and the liquid water content (LWC) are crucial for determining the optical properties of ice-free clouds (Garrett & Zhao, 2006; McFarlane & Grabowski, 2007; Slingo & Schrecker, 1982; Stephens, 1978). These low-level clouds, such as shallow boundary layer clouds (e.g., subtropical stratocumulus and trade-wind cumulus) have significant impacts on the radiation budget and climate change (Bony & Dufresne, 2005). While most past studies have focused on r_e and LWC, the relative dispersion (ϵ), defined as the ratio of the standard deviation of the droplet size distribution (σ) to the number mean radius (r_m), represents another DSD parameter which is of great importance to estimate the indirect aerosol effect on the climate system (Peng & Lohmann, 2003).

The dependence of cloud microphysical properties on environmental conditions can be investigated using optical probes capable of measuring DSDs (e.g., Burnet & Brenguier, 2007; Dong et al., 2020; McFarquhar, Zhang, et al., 2007; Y. Yang et al., 2019; Zhao et al., 2019) installed on aircraft. Using such in situ data, ϵ , r_e , and LWC can be derived from the DSDs (Heymsfield & McFarquhar, 2001; Martin et al., 1994; Stephens & Platt, 1987; Zhao et al., 2012). For instance, Arabas et al. (2009) found that ϵ , r_e , and droplet spectral width in the lowest few hundred meters above the base of shallow tropical cumuli are similar to those found in stratocumulus clouds. But, those in the upper half of the cloud field depth are substantially larger than those in stratocumulus. Nearly constant r_e values with large LWC fluctuations have been found in the upper parts of some non-precipitating convective clouds (Khain et al., 2013; Paluch & Knight, 1984). Other in situ observations and model simulations have shown that broadening mean spectral widths (i.e., the standard deviation of DSDs, σ) with height above cloud base lead to variations of r_e (Brenguier, 1998; Pinsky et al., 2014; Warner, 1969, 1973; F. Yang et al., 2018). However, despite these studies, the mechanisms leading to the variability of r_e are still not well understood (Magaritz-Ronen et al., 2016).

On the other hand, diffusion growth theory has predicted a positive correlation between ϵ and cloud droplet number concentration (N_d) (Liu & Daum, 2002; Yum & Hudson, 2005). While many studies (e.g., Desai et al., 2019; Liu et al., 2006; C. Lu et al., 2012; Pawlowska et al., 2006; J. Wang et al., 2009) have shown a negative correlation, some in situ measurements have shown neutral or unclear correlations between ϵ and N_d (Zhao et al., 2006). Using three dimensional large-eddy simulations of marine stratocumulus, M. L. Lu and Seinfeld (2006) found a decrease of ϵ with increasing aerosol number concentration due to the presence of smaller droplets associated with the higher aerosol concentrations. Recent studies by Chen et al. (2016, 2018) using an adiabatic parcel model revealed the joint dependence of relative dispersion on the aerosol concentration and vertical velocity. Thus, explanations for the relation between ϵ and N_d in marine stratocumulus must include the effects of both aerosol variations and dynamical conditions (Hudson & Yum, 1997; Peng et al., 2007). In addition, it is plausible that the presence of enhanced aerosol loading impacts the cloud dynamics (e.g., Koren et al., 2005). There is no consensus among the studies discussed above on the relative importance of these effects, and the few observational studies have been unable to distinguish between them. Thus, more observations of marine stratocumulus are necessary, especially in pristine regions, to investigate how ϵ varies with updraft velocity and aerosol loading, and to provide complementary observations for evaluating model simulations (Pawlowska et al., 2000).

The Southern Ocean (SO) is a region as close to pre-industrial conditions as exists on Earth (Seinfeld et al., 2016). Although retrievals of large amounts of supercooled liquid water (SLW) in clouds over the SO have been noted (Haynes et al., 2011; Hu et al., 2009; Huang et al., 2012, 2015; Z. Wang et al., 2019), in-situ observations of DSDs in supercooled clouds over the SO are scarce. Thus, processes contributing to the formation and dissipation of liquid water and ice particles over the SO are not well understood, and consequently, clouds over the SO are poorly represented in global climate models and reanalysis products (Naud et al., 2014; Trenberth & Fasullo, 2010). Models almost universally underestimate sunlight reflected by near surface cloud possibly due to difficulties in representing pervasive supercooled and mixed-phase boundary layer clouds (Bodas-Salcedo et al., 2016; Ceppi et al., 2014; Huang et al., 2015). To acquire an improved process-based understanding of what controls the variations of ϵ over the SO, it is important to characterize the microphysical properties of DSDs and the environmental properties where they occur (e.g., aerosol concentration and updraft velocity).

In this study, the vertical variations of characteristics of the DSDs (i.e., r_e , ϵ , N_d) are presented and the variation of ϵ with aerosol loading and vertical velocity (w) is analyzed and discussed for the prevalent SLW non-precipitating stratocumulus clouds observed over the SO during the Southern Ocean Clouds Radiation Aerosol Transport Experimental Study (SOCRATES, McFarquhar et al., 2021). SOCRATES was conducted in the region between Hobart, Australia and 62°S, and from 134°E to 163°E. The data acquired during SOCRATES and how they were processed are described in Section 2. The variations of the DSDs and the statistical analyses of the relations of ϵ with aerosol loading and vertical velocity are discussed in Section 3. The significance of the findings and principal conclusions are summarized in Section 4.

2. Data and Methods

The data used here were collected during SOCRATES with different instruments onboard the National Science Foundation (NSF)/National Center for Atmospheric Research (NCAR) Gulfstream V (GV) aircraft, including a suite of in-situ cloud probes. All these data were collected during 15 research flights which took place between January 15, and February 24, 2018.

2.1. Data

The cloud particle size distribution functions ($N(D)$) were measured by a Cloud Droplet Probe (CDP) for particles with maximum dimensions (D) between 2 and 50 μm , and a 2D-Stereo probe (2DS) nominally sizing particles with D between 10 and 1,280 μm . The 2DS data (Wu & McFarquhar, 2016, 2019) were processed using the University of Illinois/Oklahoma Optical Array Probe Processing Software (UIOOPS, McFarquhar et al., 2017, 2018). UIOOPS includes corrections for out of focus particles following Korolev (2007), and reconstructions for particles whose center is inside the photodiode array following Heymsfield and Parrish (1978). All particles with inter-arrival times below a time varying threshold are assumed to be shattered artifacts and hence are eliminated (Field et al., 2006). Given the large uncertainties (up to more than 100%) in the probe's depth of field for small size particles (Baumgardner & Korolev, 1997), particles with $D < 50 \mu\text{m}$ for the 2DS were not included in the analysis. Numerous morphological properties were determined for individual particles such as D , projected area, and perimeter, with particle habit identified following the modifications to Holroyd (1987) introduced in UIOOPS. In addition, angular light scattering measurements (Schnaiter, 2018; Schnaiter et al., 2018) acquired by the Particle Habit Imaging and Polar Scattering probe (PHIPS, Abdelmonem et al., 2016) were used to discriminate ice particles from droplets. Note that using high time resolution data better characterizes the small-scale cloud structure, but increases the statistical uncertainties due to fewer numbers of particle counts. A longer averaging period gets a more statistically significant measurement (e.g., McFarquhar, Timlin, et al., 2007). In this study, the number concentration and $N(D)$ represent one second averages due to the large horizontal variability noted by Y. Wang et al. (2020) even though the statistical uncertainty is larger than that associated with 5 or 10 s averages commonly used for in situ studies.

Considering all the uncertainty sources for CDP measurements (e.g., Mie ambiguity, coincidence, collection angles, etc.), the average uncertainty in sizing and concentration is $\sim 30\%$ and $\sim 20\%$, respectively (Baumgardner et al., 2017). For the 2DS measurements, the uncertainty in sizing and concentration, with the corrections made using UIOOPS, is a maximum of respectively $\sim 20\%$ ($\sim 50\%$) and $\sim 50\%$ ($\sim 100\%$) for particles with $D > 100 \mu\text{m}$ ($D < 100 \mu\text{m}$) (Baumgardner et al., 2017). The smaller the particle, the greater the uncertainty in the concentration from a photodiode probe (Baumgardner & Korolev, 1997), such as the 2DS. Note that the standard deviation and dispersion were calculated from the CDP measurements which defines the DSD with $3 < D < 50 \mu\text{m}$. The $N(D)$ for $50 < D < 100 \mu\text{m}$ measured by the 2DS was not included in the calculation of the standard deviation and dispersion because the uncertainties for $N(D)$ in this size range from the 2DS are much larger than those from the CDP. But, in any event, $N(D)$ for $50 < D < 100 \mu\text{m}$ are sufficiently small that their inclusion would have resulted in little changes to the relative dispersion value ($< 3\%$ for all cases). Thus, uncertainties from the 2DS were not included in the DSD uncertainty. Given the average uncertainty in sizing and concentration of $\sim 30\%$ and $\sim 20\%$ in the CDP, uncertainties in the standard deviation and relative dispersion of DSD are $\sim 14\%$ and $\sim 25\%$, respectively, using root-sum-squared error propagation.

The aerosol size distribution ($N(D_p) = dN/d\log D_p$) was measured by a wing pod-mounted Ultra High Sensitivity Aerosol Spectrometer (UHSAS) for particle optical diameter (D_p) between 0.06 and 1 μm . The UHSAS has a collection efficiency of $\sim 100\%$ for $D_p > 100 \text{ nm}$ and concentrations below $3,000 \text{ cm}^{-3}$ (Cai et al., 2008). To avoid sample flow issues related to pressure variations during aircraft altitude changes, the routings of the tubing for pump, sheath flow and exhaust were modified for better performance during altitude profiles, and volume flow controllers were used to maintain constant volumetric sheath flows. With the above modifications, the UHSAS instrument is capable of making accurate (ranging from 7% for $D_p < 0.07 \mu\text{m}$ to 1% for $D_p > 0.13 \mu\text{m}$ for sizing), precise ($< \pm 1.2\%$ for number counting), and continuous (1 Hz) measurements of size-resolved particle number concentration at ambient pressures from 225 to 1,013 hPa (Kupc et al., 2018).

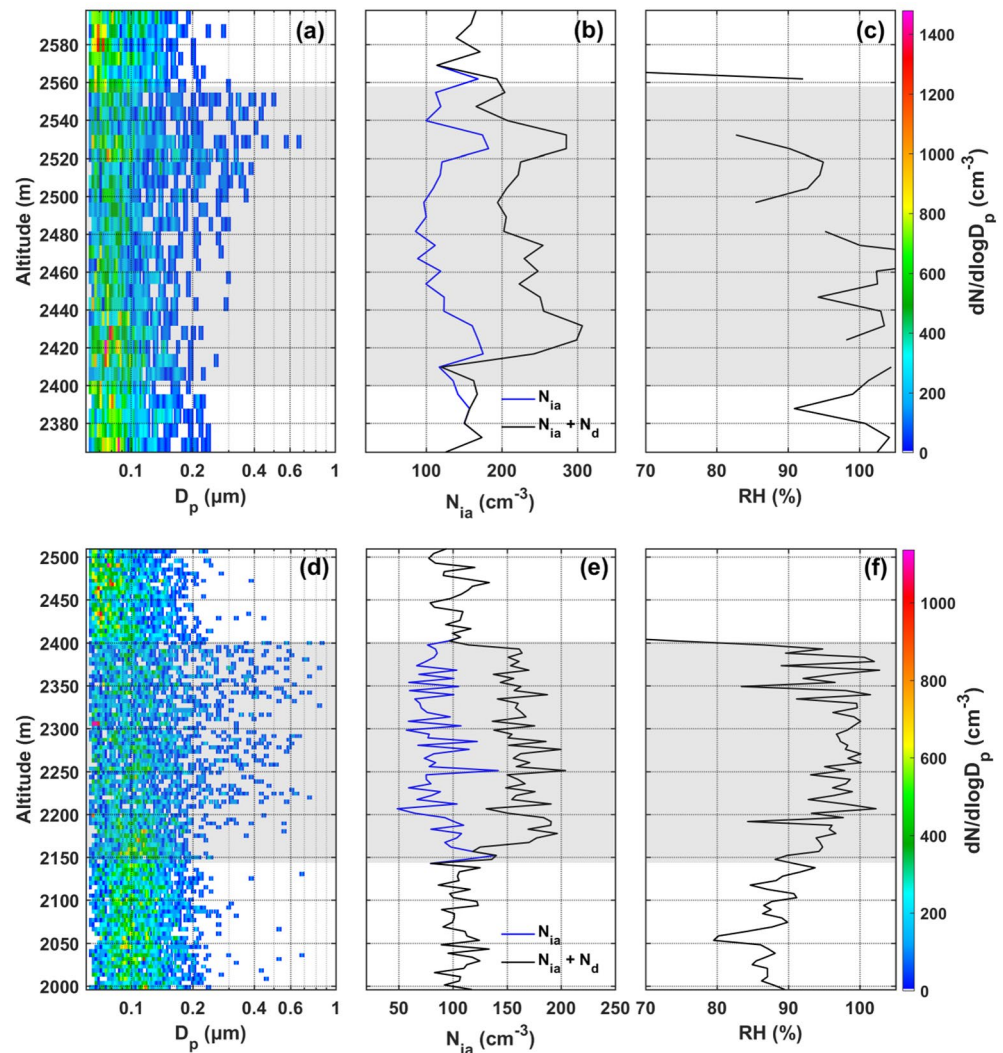


Figure 1. Vertical profiles of $N(D_p)$ (a and d), N_{ia} and $N_{ia} + N_d$ (b and e) and relative humidity (RH) with respect to water (c and f) for two stratocumulus penetrations. Figures (a–c) were measured at 03:30 on 20180124 (UTC) (Case No. 13 in Table S1) and Figures (d–f) were measured at 00:59 on 20180208 (UTC) (Case No. 22 in Table S1). The gray shades indicate the identified locations of the cloud layer. There are some missing RH values in Figure R3c.

In this study, particles with D_p between 0.06 and 0.5 μm measured by the UHSAS inside the clouds were assumed to be interstitial aerosol particles following J. Wang et al. (2009). The interstitial aerosol concentration (N_{ia} hereafter) was used to define the aerosol loading levels. Because the UHSAS inlet is susceptible to shattering, only samples in ice-free stratocumulus were used. Even so, residual particles might be counted in N_{ia} . Therefore, N_{ia} should be regarded as an upper bound for interstitial aerosol concentrations in this study. Figure 1 shows the vertical variations of $N(D_p)$ and N_{ia} below, within and above the cloud layer for two penetrations during SOCRATES. The N_{ia} variations behave differently with altitude, either increasing or slightly decreasing with height due to different aerosol hygroscopic growth rates and other factors (e.g., activation and coagulation) influencing the concentrations with D_p between 0.060 and 0.5 μm . The vertical variations of N_{ia} below and within cloud were examined for all cloud penetrations (Figure S1). They show good consistency and the difference between them is $\sim 28 \text{ cm}^{-3}$ on average. Thus, N_{ia} is used as a proxy for the level of aerosol loading in this study.

The bulk LWC was measured by a Commonwealth Scientific and Industrial Research Organisation (CSIRO) King probe (King et al., 1978) which has a 15% uncertainty (King et al., 1985). The LWC measured by the

King probe was compared with that derived from the CDP DSD and shows good consistency (R^2 of the linear fit is 0.95). Therefore, the LWC in this study refers to that measured by the King probe.

The presence of SLW was identified using a Rosemount Icing Detector (RICE), with a voltage change of 2 mV s^{-1} indicating SLW at temperatures less than $-4 \text{ }^\circ\text{C}$ (Cober et al., 2001). The RICE could not detect the presence of SLW at higher temperatures due to the dynamic heating of the probe (Cober et al., 2001; McFarquhar, Zhang, et al., 2007). In this study, SLW was first identified for each second of flight using the RICE measurement for temperatures below $-4 \text{ }^\circ\text{C}$ and the 2DS/PHIPS habit information for temperatures above $-4 \text{ }^\circ\text{C}$.

The data from the CDP, King, UHSAS and RICE probes, and all other data sets (e.g., the temperature (T), vertical velocity (w) from the radome wind system onboard the aircraft) used in this study were processed at the NCAR Research Aviation Facility (RAF) and were included in the product: “Low Rate (1 Hz) Navigation, State Parameter, and Microphysics Flight-Level Data” (UCAR/NCAR-Earth Observing Laboratory, 2018). The net uncertainty in the standard measurement of w is 0.12 m s^{-1} applies to individual 1-Hz measurements and these data are only deemed reliable when the absolute value of the aircraft roll is less than 5° for typical profile samplings (Cooper et al., 2016).

2.2. Method

For the period of all SOCRATES flights, the flight track and image from the forward-looking camera onboard the aircraft were overlaid on satellite images (e.g., Figure S3) for every 15 min. The corresponding altitude-time cross section (e.g., Figure S4) of reflectivity, radial velocity, linear depolarization ratio (LDR) and spectral width measured from High-Performance Instrumented Airborne Platform for Environmental Research (HIAPER) cloud radar (HCR), and the altitude-time cross section of particle depolarization ratio measured from the High Spectral Resolution Lidar (HSRL) were also generated for each 15 min of flight. Based on these figures, all time periods during SOCRATES corresponding to ascents and descents through closed-cell stratocumulus clouds were identified. Then every stratocumulus cloud profile from these penetrations with the presence of SLW was used in the analysis. Cloud profiles in warm clouds with $T > 0$ were also included. Among these flight profiles, most of them were incomplete or contaminated by the coupled lower cumulus clouds which were frequently seen beneath the stratocumulus layers over the midlatitude ocean regions (Wyant et al., 1997).

A point was determined to be within the cloud if the N_d from the CDP was larger than 10 cm^{-3} (McFarquhar, Zhang, et al., 2007; Zhao et al., 2018). To restrict analysis to clouds without influence from large ice or rain precipitating particles, any profile with the presence of ice particles or large rain droplets ($D > 200 \text{ }\mu\text{m}$) identified by the 2DS/PHIPS was not included in the analysis. Of 51 profiles, 15 ($\sim 30\%$) were found to have precipitation and hence were excluded. Therefore, only several complete profiles without contamination from other clouds were included in the statistical analysis after excluding profiles with precipitation. That is why many of those 11 flights yielded only one or two such profiles. In the end, a total of 36 shallow stratocumulus profiles was thus used in this study (see Table S1). Within the remaining 36 profiles, 12 of 36 profiles ($\sim 33\%$) had light drizzle with some droplets with $50 < D < 200 \text{ }\mu\text{m}$. But the drizzle droplet concentrations ($50 < D < 200 \text{ }\mu\text{m}$) obtained from 2DS for these profiles were less than 0.2 cm^{-3} and hence assumed to be non-precipitating following M. L. Lu et al. (2008).

3. Results and Discussion

3.1. The Properties of a Stratocumulus Cloud Profile

Figure 2 shows an example of a SLW stratocumulus profile depicting microphysical properties below, within and above the cloud layer at a location around 53.6°S , 137.4°E at 00:12 UTC on January 23, 2018. As shown in Figure 2a, the cloud base and top altitudes are at about 2,920 and 3,230 m with temperatures around $-14.7 \text{ }^\circ\text{C}$ and $-16.7 \text{ }^\circ\text{C}$, respectively. An inversion layer exists just above cloud top. In this case, the concentration of large droplets ($> 50 \text{ }\mu\text{m}$) is quite small (0.003 cm^{-3}), and the ratio of LWC calculated from this size range to the LWC measured by the King probe is only 0.3%, suggesting negligible impact of these particles on LWC. The growth of droplets with height appears within several tens of meters above cloud

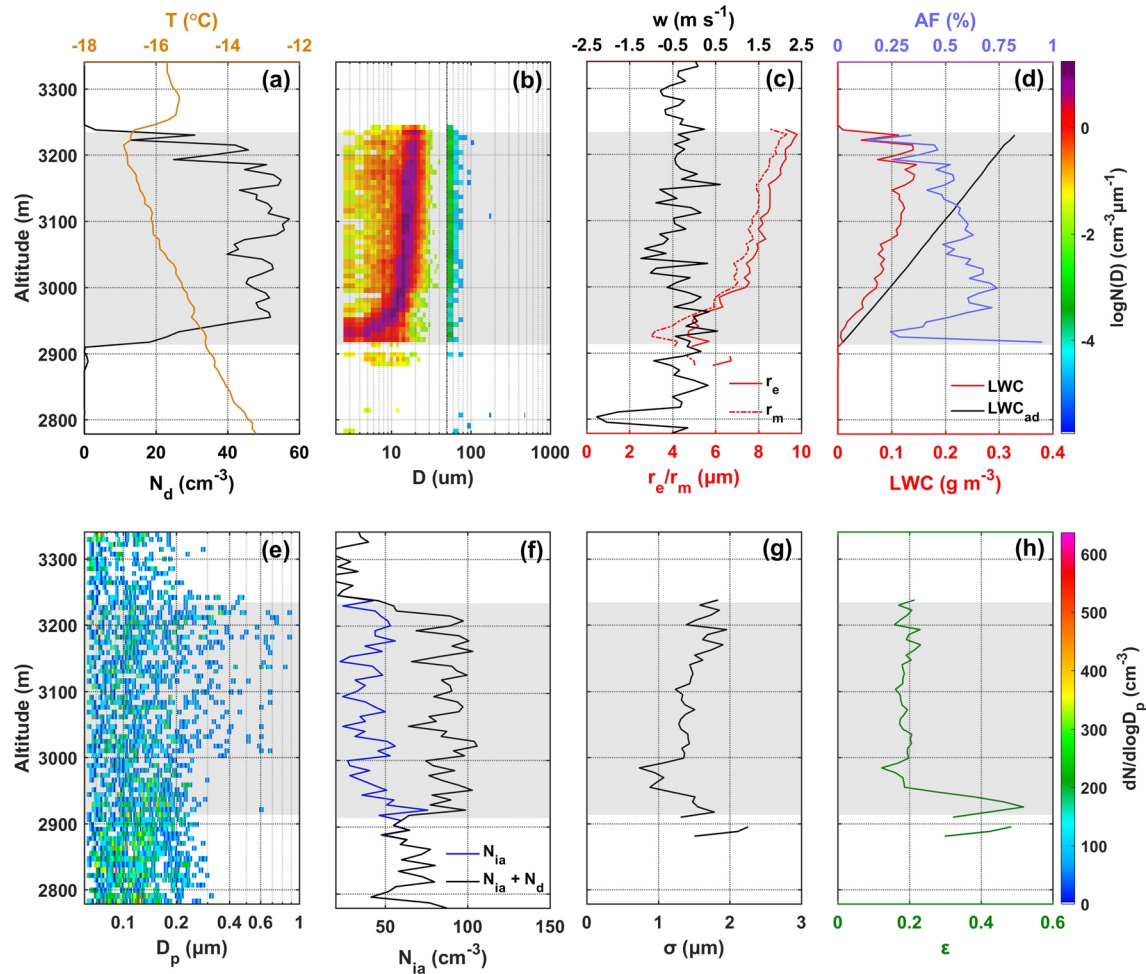


Figure 2. A stratocumulus cloud profile measured around 53.6°S, 137.4°E on 00:12 UTC on January 23, 2018 (Case No. 9 in Table S1) for the microphysical parameters of (a) N_d and T , (b) $N(D)$ (CDP for $D < 50 \mu\text{m}$ and 2DS for $D > 50 \mu\text{m}$), (c) w , r_e and r_m , (d) LWC, adiabatic LWC (LWC_{ad}) and adiabatic fraction ($\text{AF} = \text{LWC}/\text{LWC}_{\text{ad}}$), (e) $N(D_p)$ from UHSAS, (f) N_{ia} and $N_{\text{ia}} + N_d$, (g) σ , and (h) ϵ . The gray shading indicates the location of the cloud layers. The black dashed line in (a) represents $D = 50 \mu\text{m}$.

base (Figure 2b). As shown in Figure 2c, the w in the cloud fluctuates between -1.2 and 0.6 m s^{-1} with a mean and standard deviation of -0.33 and 0.42 m s^{-1} . Though the radial growth rate slows for higher altitudes above cloud base, r_e and r_m synchronously increase with height (Figure 2c) while N_d is near constant ($\sim 50 \text{ cm}^{-3}$) with the decrease near cloud top likely due to entrainment. These features are consistent with the theoretical predictions of diffusional growth (e.g., Liu et al., 2006). Note that r_e first decreases around cloud base and then begins to monotonically increase at higher altitude.

The adiabatic LWC (LWC_{ad}) is derived as a function of cloud temperature, pressure and cloud base following Brenguier (1991). The adiabatic fraction (AF, defined as $\text{LWC}/\text{LWC}_{\text{ad}}$) in Figure 2d shows that the measured LWC is close to the LWC_{ad} at heights around cloud base and decreases gradually at higher altitudes, indicating that entrainment at cloud top and subsequent dilution and evaporation of cloud droplets are occurring.

For aerosols, on the other hand, $N(D_p)$ in Figure 2e below cloud base is similar to that near cloud base. Similar behavior is noted for other cases. However, there are many specific reasons for the different behaviors of N_{ia} within the cloud. Although most particles smaller than $0.1 \mu\text{m}$ might remain unactivated inside cloud, aerosol particles too small for UHSAS to initially measure are hydrating and growing in cloud, which would allow them to be counted thereby increasing N_{ia} within the cloud, especially for particles with $D_p < 0.06 \mu\text{m}$. These smaller particles account for the considerable amount of the total aerosol concentration. The $N(D_p)$ in Figure 1a clearly shows that $\sim 30\%$ more particles (below $0.1 \mu\text{m}$) are in the higher part of cloud. In addition,

cloud drops could be potentially evaporated to form interstitial aerosols. But, deactivation may also occur because particles occur in the entrainment mixing or circulation mixing conditions previously noted by J. Wang et al. (2009), and hence are exposed to low supersaturation (below the particle equilibrium supersaturation). This is consistent with the lower RH (Figure 1c) in the higher part of clouds. The slight decrease of N_{ia} at some altitudes is also consistent with the activation, coagulation, and scavenging process. Note also that a few large drizzle droplets with $D > 50 \mu\text{m}$ are commonly seen suggesting that the scavenging process may play a role in the decrease of N_{ia} with height. Additionally, variation in aerosol sizes and hygroscopic properties will affect nucleation which may also contribute to N_{ia} variability Earle et al. (2011). Although it is known that these processes together lead to the vertical variation of N_{ia} (Figures 1, 2e, and 2f), there is not sufficient information to quantitatively determine the role of each process.

Though r_e and r_m monotonically increase with height, σ varies between approximately 1 and 2 μm (Figure 2g) and ϵ decreases rapidly with height from ~ 0.5 (at cloud base) to ~ 0.2 (100 m above base) and then remains relatively constant to cloud top (Figure 2h). This shows good agreement with the simulated condensation process (Brenguier, 1991; Khain et al., 2000), which predicts a linear increase of r_e and a small ϵ variation of 0.15–0.25 around cloud top.

3.2. Mean Statistics of Stratocumulus Profiles Over the SO

Figure 3 summarizes the profiles of cloud properties averaged over the selected stratocumulus penetrations as listed in Table S1. Following McFarquhar, Zhang, et al.'s (2007) analysis of Arctic cloud profiles, the altitude in cloud (Z_n) has been normalized by setting the cloud base as 0 and cloud top as 1. The averaged

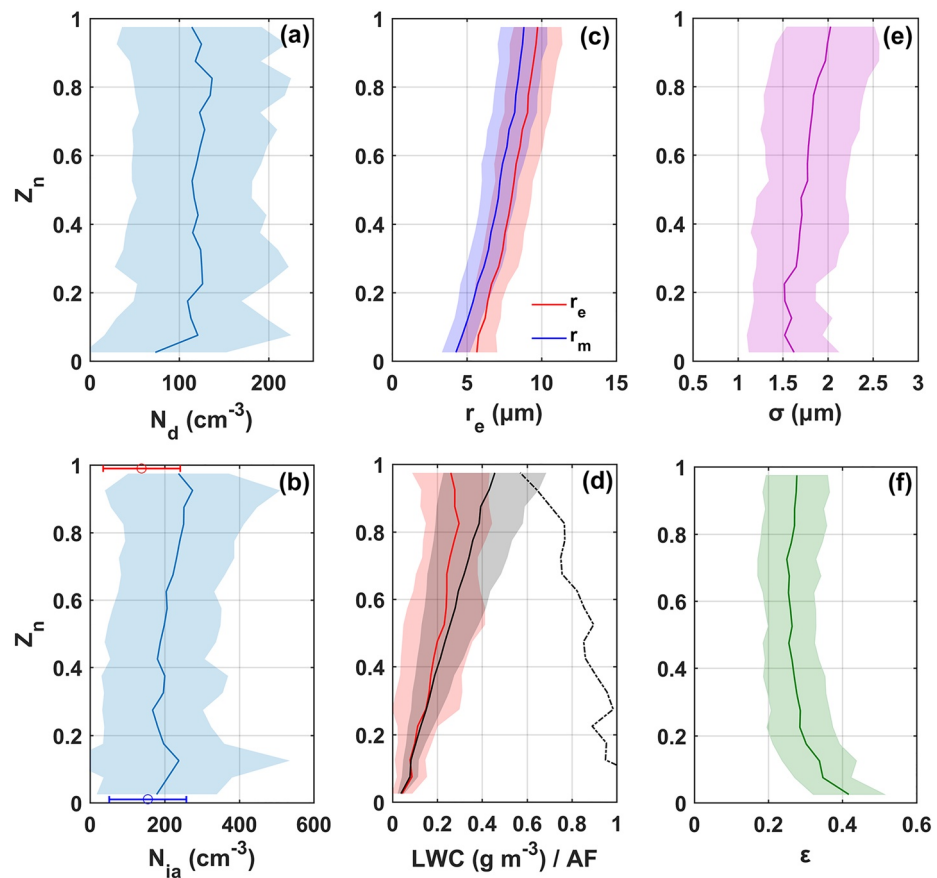


Figure 3. Averaged profiles as a function of normalized cloud depth (Z_n) of (a) N_d , (b) N_{ia} , (c) r_e and r_m , (d) LWC, LWC_{ad} and the mean AF (black dashed line), (e) σ , and (f) ϵ . The shaded regions indicate one standard deviation. The blue (red) error bar represents the mean and standard deviation of N_{ia} with 50–150 m below cloud base (above cloud top).

cloud base height (depth) and temperature are $1,512 \pm 805$ m (251 ± 113 m) and -8.4 ± 6.5 °C, respectively. For all cloud profiles analyzed here, the LWC integrated for droplets with D between 50 to 200 μm accounts for 0.22% of the LWC from the King probe on average, implying that drizzle makes little contribution to the LWC. The average N_d in the shallow stratocumulus clouds over the SO is 112.8 ± 64.5 cm^{-3} with a concentration of 83.1 ± 72.3 cm^{-3} at cloud base and 99.4 ± 87.1 cm^{-3} at cloud top (Figure 3a). The average N_{ia} (214 ± 169 cm^{-3}) varies little with Z_n , with a slight increase from 182 ± 161 cm^{-3} at cloud base to 216 ± 133 cm^{-3} at cloud top (Figure 3b). As indicated earlier, the consistency of N_{ia} below and within cloud makes it a good proxy for the upper bound of aerosol loading and suggests that cloud droplets do not interfere substantially with that estimate. Figure 3b shows a peak value around $Z_n = 0.1$, consistent with the peak location of N_d near cloud base. This is consistent with the hygroscopic growth of aerosols smaller than those measured by the UHSAS being more than offset by activation across all cases. Figures 1a–1c show an example that show the results are consistent with more than 100 cm^{-3} particles being activated near cloud base with N_{ia} also increasing especially for N_{ia} with $D_p < 0.1$ μm near cloud base. Both N_{ia} and N_d increase very slightly with altitude, which could be caused by the entrainment of above-cloud air with high N_{ia} (close to the N_{ia} below the cloud base), leading to increases in cloud condensation nuclei and the subsequent increase of N_d within cloud top. Both N_{ia} and N_d observed over the SO are much smaller than that over other regions (J. Wang et al., 2009; Wood, 2012; Zhao et al., 2006). For example, N_d and N_{ia} observed by J. Wang et al. (2009) in the eastern Pacific are about twice those over the SO, indicative of the clean environment over the SO.

As shown in Figure 3c, the average r_e increases nearly monotonically from 5.3 ± 1.9 μm at cloud base to 9.4 ± 2.2 μm at cloud top. The r_m profile synchronously varies with r_e and is ~ 1.2 μm smaller than r_e on average. The LWC (Figure 3d) increases linearly from cloud base and decreases near cloud top with a mean LWC of 0.17 ± 0.14 g m^{-3} . The average AF is close to 1 around cloud base and decreases to 0.56 ± 0.41 near cloud top, consistent with entrainment, dilution and evaporation occurring near cloud top.

The spectral width (σ , Figure 3e) slightly increases as the droplet spectra broaden with height, which could be related to evaporation due to inhomogeneous entrainment-mixing and/or secondary activation of aerosol entrained into clouds (e.g., C. Lu et al., 2020; Yeom et al., 2019). This is consistent with the multiple peaks in the cloud DSD near 3 μm , and an additional cluster of secondary peaks between 5 and 8 μm near cloud top (just below 3,200 m) in Figure 2b. The variation of σ is small on average (~ 1.1 – 2.6 μm), consistent with the study of Pawlowska et al. (2006). Figure 3f shows that the averaged ϵ decreases from 0.42 ± 0.13 at cloud base to a relatively constant value of 0.27 ± 0.09 at upper heights. These ϵ values are close to the observations for clouds in pristine marine regions (McFarquhar & Heymsfield, 2001; Politovich, 1993), and ~ 0.1 – 0.2 smaller than those observed in polluted marine and polluted continental regions (e.g., Martin et al., 1994; Miles et al., 2000). Combined with the large adiabatic fraction from cloud center to cloud top (Figure 3d), this suggests a small difference in ϵ between near-adiabatic (cloud center) and diluted cloud (cloud top) regions and the broadening processes (e.g., inhomogeneous entrainment-mixing and/or secondary activation) may have little impact on dispersion, consistent with the observations of Pawlowska et al. (2006).

3.3. The Impact of the N_{ia} and w on the Relative Dispersion

To investigate the impacts of vertical velocity and aerosols on the relative dispersion of DSDs, Figure 4a shows the relationship of ϵ with N_d , w , and N_{ia} . For low aerosol loading ($N_{ia} < 100$ cm^{-3}), the N_d is also < 100 cm^{-3} and ϵ shows a strong negative correlation with N_d . For high aerosol loading ($N_{ia} > 300$ cm^{-3}), however, the $N_d > 200$ cm^{-3} and ϵ shows a positive correlation with N_d . The black line, representing the average ϵ for each N_d bin, clearly shows the relationship between ϵ and N_d for both low and high aerosol loading conditions. The analytical expression in Liu et al. (2006) theoretically demonstrates that aerosol loading leads to an increase of ϵ (positive correlation) whereas enhanced updrafts lead to smaller ϵ (negative correlation), both of which affect the ϵ - N_d relation. The negative ϵ - N_d relation when $N_d < 100$ cm^{-3} from Figure 4 is consistent with many previous studies (C. Lu et al., 2012; Miles et al., 2000; Peng et al., 2007; Sinclair et al., 2020; J. Wang et al., 2009), whereas the positive correlation at higher N_d (e.g., Chen et al., 2018; Liu & Daum, 2002; Liu et al., 2006; Peng et al., 2007; Yum & Hudson, 2005) is dominated by the effect of aerosol loading because

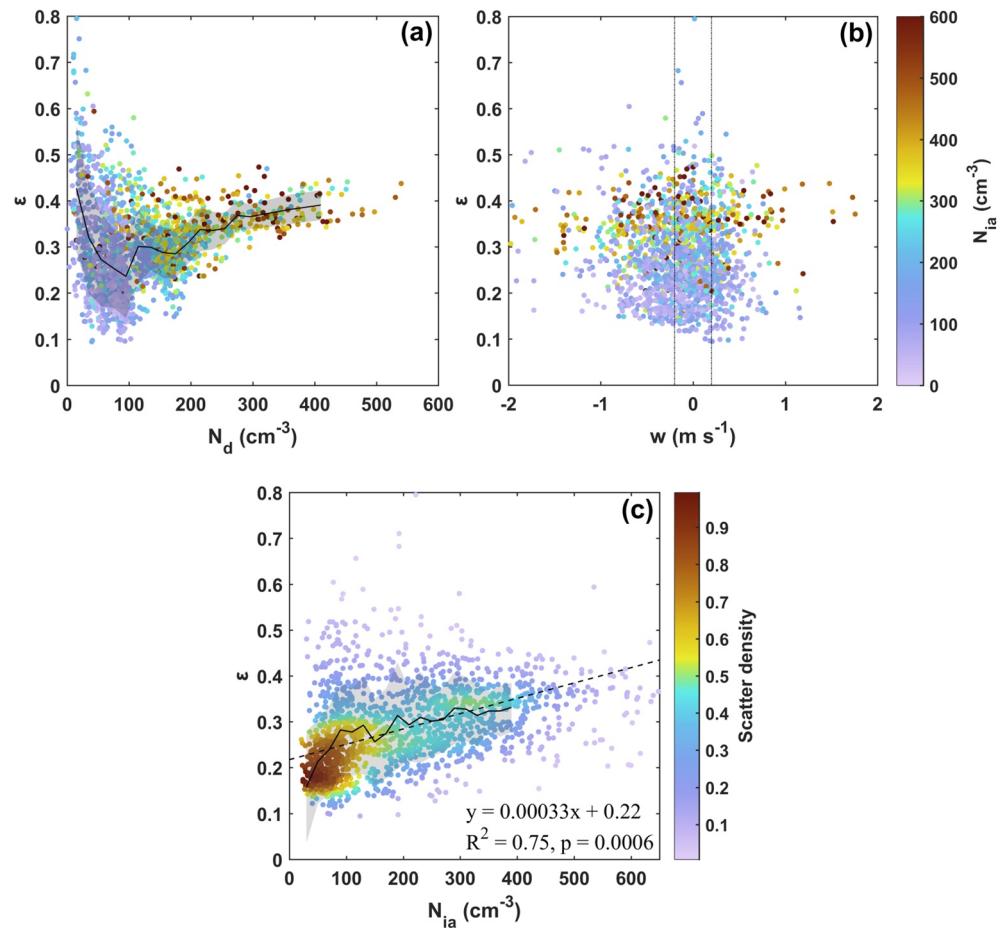


Figure 4. ϵ as a function of (a) N_d , (b) w , and (c) N_{ia} . (a) and (b) are colored by N_{ia} and (c) by the scatter density (with the densest as 1). The solid black line and gray shade area in (a) and (c) show the mean and standard deviation of ϵ in each bin of N_d and N_{ia} . The dashed black lines in (b) represent $w = -0.2 \text{ m s}^{-1}$ and $w = 0.2 \text{ m s}^{-1}$, respectively. The dashed black line in (c) represents the linear fit for the black line and the text shows the linear fit function, R^2 , and p value. Each point represents a 1-s average.

w over SO stratocumulus is low (nearly 80% of w is between -0.5 and 0.5 m s^{-1} , see also Figure S2). Note that Sinclair et al. (2020) used a different technique to remotely measure the cloud droplet size distribution, which may offer additional credence to our finding. Figure 4c demonstrates such significant positive ϵ - N_{ia} correlation regardless of the w variations. A previous modeling study (Peng et al., 2007) indicated that the positive correlation between ϵ and N_d due to the aerosol effect was weakened with increasing w , and would disappear when w is larger than 0.55 m s^{-1} . Thus, the negative effect of w on ϵ is not significant due to the weak w conditions measured during SOCRATES, leading to a positive ϵ - N_d relation when $N_d > 200 \text{ cm}^{-3}$. The combined aerosol and dynamical effects result in a convergence in ϵ (e.g., Zhao et al., 2006) which is implied by the considerable scatter of ϵ with N_{ia} between 100 and 300 cm^{-3} in Figure 4a.

In order to determine how the vertical structure varies with other parameters, Figure 5 shows N_d (a, e, i), ϵ (b, f, j), σ (c, g, k), and r_m (d, h, l) as a function of N_{ia} for each profile averaged around cloud top (a–d), cloud base (e–h), and the entire profile (i–l). The cloud top (cloud base) samples were determined when $Z_n > 0.8$ ($Z_n < 0.2$). All the parameters show similar trends both in the cloud top and cloud base regions. As to the impact of N_{ia} on N_d , it is not surprising to see a more distinct (significant with $p < 0.05$) linear relationship at cloud base, with a higher coefficient of determination (R^2) and slope compared to those at cloud top. This could be induced by the influence of w around cloud base. On the other hand, other processes (e.g., entrainment and evaporation) weaken the relation of N_{ia} to N_d at cloud top. Nevertheless, for the entire cloud

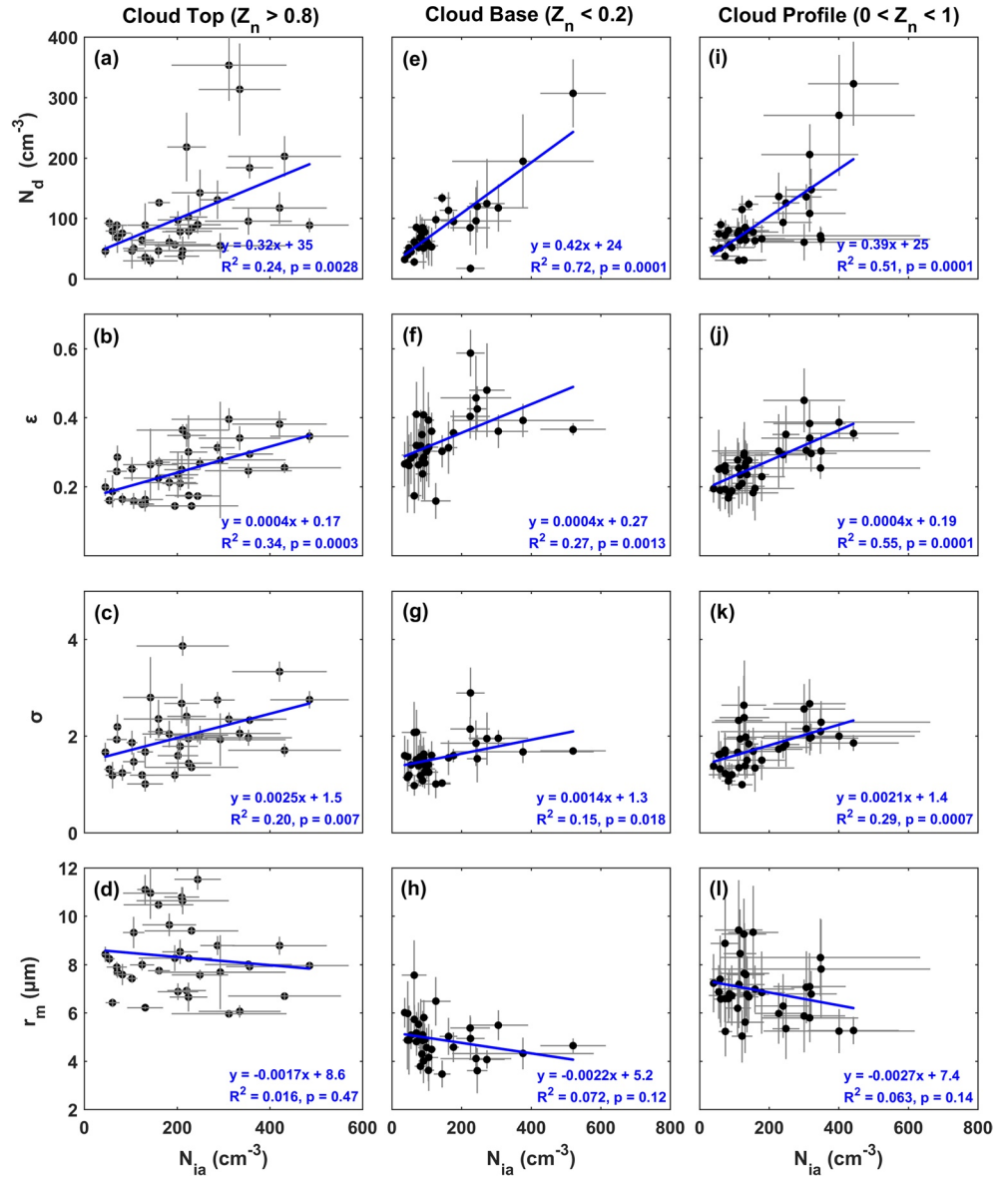


Figure 5. N_d (a, e, i), ϵ (b, f, j), σ (c, g, k), and r_m (d, h, l) as a function of N_{ia} for each profile, with averages computed for points around cloud top (a–d), around cloud base (e–h) and entire profile (i–l). The black points and gray lines show the mean values and the standard deviations (at both corresponding axis), respectively. For each panel, the solid blue line represents the linear fit and the text shows the linear fit function, R^2 , and p value.

profile, the effect of N_{ia} on N_d is still evident and significant. Though the w over SO stratocumulus is low (Figure S2), it is worth noting that the effect of w is not actually separated out in Figure 5. This could be the reason why the variation of N_{ia} can explain 72% (R^2) of the N_d variation in Figure 5e.

The relations of ϵ to N_{ia} around the cloud top and cloud base are similar (Figure 5b, 5f, and 5j) but with lower R^2 value compared to the effect of N_{ia} on N_d . This shows a dominant impact of N_{ia} on N_d with the weaker effect of N_{ia} on ϵ suggesting the joint dependence of N_{ia} and w on ϵ as noted by previous studies (Chen et al., 2018; C. Lu et al., 2012). Stronger updrafts at cloud base weaken the effect of N_{ia} on ϵ compared to the conditions in cloud top as seen in Figure 5b and 5f. As a whole, the variation of N_{ia} can explain 55% (R^2) of the ϵ variation (Figure 5j). The significant positive relation of σ to N_{ia} and the insignificant negative relation of r_m to N_{ia} show that the effect of N_{ia} on σ dominates the N_{ia} - ϵ relation.

To further isolate the effect of cloud dynamics from aerosol loading, samples in a small bin of w with $-0.2 \text{ m s}^{-1} < w < 0.2 \text{ m s}^{-1}$ (dashed lines in Figure 4b) were used to investigate the aerosol effect on the relative dispersion of DSDs for areas without appreciable updrafts. This small w range was set considering the w measurement uncertainties (0.12 m s^{-1} as discussed in Section 2) to correspond to instances with minimal, if any, vertical motion. Figures 6a–6c show the results of how ϵ varies with N_{ia} using several different small bins of w and the entire data set. For the relatively limited range of w , ϵ shows a significant increase with increased aerosol loading, indicating the dominant positive effect of N_{ia} on dispersion when w is small.

Figures 6d–6f show the sensitivity of ϵ to w for different narrow ranges of N_{ia} . The range of N_{ia} ($60\text{--}100 \text{ cm}^{-3}$) in Figure 6d is set as close to the pristine aerosol loading as possible while including enough samples to be considered statistically significant. Figure 6d shows a significant (F -test) decrease of ϵ with increasing w when nearly excluding the effect of aerosols. This negative relation between ϵ and w becomes weak when the aerosol loading is higher, especially when N_{ia} is larger than $\sim 270 \text{ cm}^{-3}$. These observations over the SO for the ϵ - w relationship under different aerosol conditions are consistent with the simulations of Peng et al. (2007), indicating approximately equivalent but contrasting effects of vertical velocity and aerosol loading on ϵ over this region.

Though the discussions (at the end of Section 3.2) offer an insight as to why a small difference in ϵ between near-adiabatic (cloud center) and diluted cloud (cloud top) regions and the broadening processes (e.g., inhomogeneous entrainment-mixing and/or secondary activation) may have little impact on dispersion, further analyses discussed below tries to exclude these influencing factors. Because the decrease of adiabatic fraction with height suggests that other dynamic processes such as entrainment and evaporation around cloud top are much stronger than near the cloud base, samples near cloud base region are analyzed to limit factors other than vertical velocity to investigate effects of N_{ia} (or w) on ϵ . It is not surprising that Figures 7a–7c shows similar results on how ϵ varies with N_{ia} as in Figures 6a–6c as there is a limited range of w

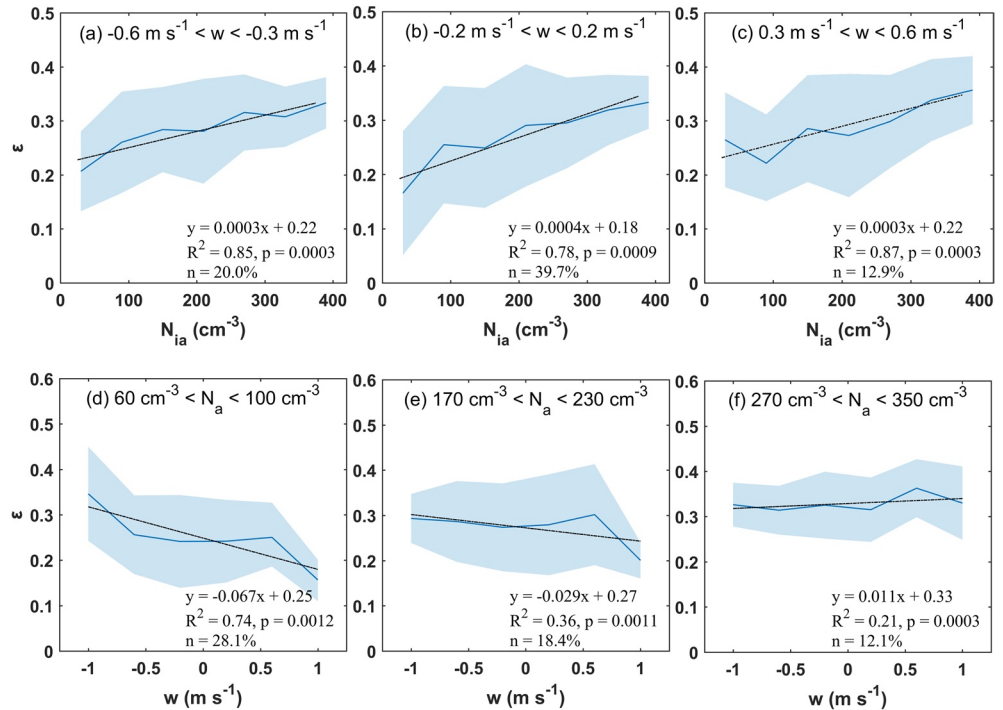


Figure 6. ϵ as a function of N_{ia} for w ranges of (a) $-0.6 \text{ m s}^{-1} < w < -0.3 \text{ m s}^{-1}$, (b) $-0.2 \text{ m s}^{-1} < w < 0.2 \text{ m s}^{-1}$ and (c) $0.3 \text{ m s}^{-1} < w < 0.6 \text{ m s}^{-1}$ and ϵ as a function of w for N_{ia} ranges of (d) $60 \text{ cm}^{-3} < N_{ia} < 100 \text{ cm}^{-3}$, (e) $170 \text{ cm}^{-3} < N_{ia} < 230 \text{ cm}^{-3}$, and (f) $270 \text{ cm}^{-3} < N_{ia} < 350 \text{ cm}^{-3}$. All the samples were included ($0 < Z_n < 1$). The blue lines and shaded regions indicate the mean and one standard deviation. The black dashed lines represent the linear fits and the text in each box shows the linear fit function, R^2 , p value, and the relative percentage (n) of each subsample size.

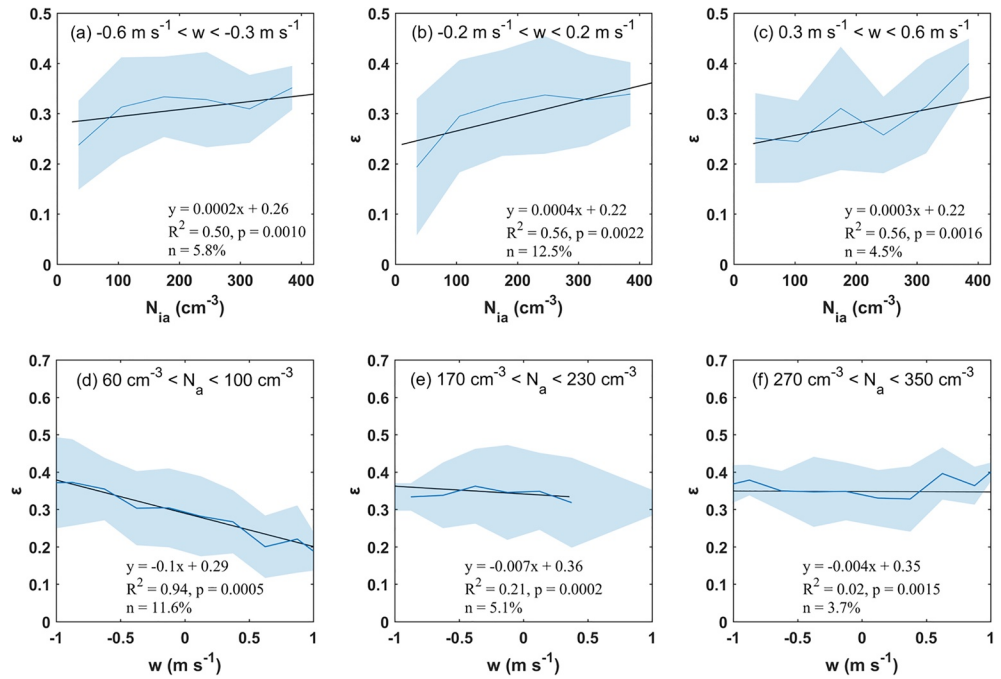


Figure 7. As in Figure 6 but for samples measured near cloud base ($Z_n < 0.2$).

in each panel. Figures 7d–7f show the relations of ϵ to w near cloud base for different N_{ia} ranges of 60–100, 170–230, and 270–350 cm^{-3} , respectively. For low aerosol loading ($N_{ia} < 100 \text{ cm}^{-3}$), it is evident that the relative “net” effect of w on ϵ is significantly negative with higher R^2 and slope compared to the entire cloud profile averaged condition shown in Figure 6d. When aerosol loading increases, this negative relationship becomes weaker. Furthermore, cloud top samples (figure not shown) are consistent with the interpretation of a minor influence of inhomogeneous entrainment-mixing and/or secondary activation on the dispersion. M. L. Lu and Seinfeld (2006) also found that the effect of entrainment mixing on dispersion is not significant using model simulations.

To summarize, the previously noted dependence of ϵ on w has been confirmed over the pristine SO, but the decreasing rate shown here is slightly higher than the value observed by Berg et al. (2011) over polluted land areas. The magnitude of the change of ϵ to N_{ia} is comparable to that of ϵ to w , suggesting a strong sensitivity of ϵ to aerosol concentrations in this pristine environment. This might explain why a distinct positive ϵ relation to aerosols exists over the pristine SO while no discernable aerosol effects on ϵ were observed in other regions (e.g., M. L. Lu et al., 2008; Zhao et al., 2006).

4. Conclusions

Ubiquitous supercooled liquid stratocumuli were observed over the Southern Ocean (SO) during SOCRATES using in-situ aircraft measurements. The characteristics of the DSDs and the statistical relations of relative dispersion (ϵ) with vertical velocity (w) and interstitial aerosol concentration (N_{ia}) were investigated using 36 non-precipitating stratocumulus profiles. The average cloud droplet effective radius (r_e) increased nearly monotonically from $5.3 \pm 1.9 \mu\text{m}$ at cloud base to $9.4 \pm 2.2 \mu\text{m}$ at cloud top with N_d remaining relatively constant. The ϵ decreased rapidly from cloud base (with the mean of 0.42 ± 0.13) and remained relatively constant from near-adiabatic (cloud center) to diluted cloud (cloud top) regions with a mean value of 0.27 ± 0.09 . The vertical structure of cloud properties found here for stratocumulus clouds in the pristine SO environment, provides useful information for parameterizations of supercooled DSDs in stratocumulus and the estimation of aerosol indirect effects over the pristine SO.

The ϵ increases (decreases) with increasing N_{ia} (w) for a small range of w (low N_{ia}) at a 95% confidence level. Although numerous factors contribute to the DSDs properties, this study demonstrates the importance of

the roles of aerosol and cloud dynamics on ϵ , which is crucial to the estimation of aerosol indirect radiative forcing, especially for the pristine SO regions, where models almost universally underestimate the reflected radiation. This work will be particularly useful in a physical understanding that ultimately be helpful for parameterization development and their interaction with aerosols and updrafts for shallow ice-free strato-cumulus in the future.

Data Availability Statement

The data were collected using NSF's Lower Atmosphere Observing Facilities, which are managed and operated by NCAR's Earth Observing Laboratory. The NSF SOCRATES campaign data set is publicly available and can be accessed at http://www.eol.ucar.edu/field_projects/socrates.

Acknowledgments

This work was supported by the Ministry of Science and Technology of China National Key R&D Program (2019YFA0606803), the National Natural Science Foundation of China (41925022, 41575143), the State Key Laboratory of Earth Surface Processes and Resource Ecology, and the United States National Science Foundation (grant nos. 1628674 and 1762096). This material is based upon work supported by the National Center for Atmospheric Research, which is a major facility sponsored by the National Science Foundation under Cooperative Agreement No. 1852977. The authors thank the pilots, mechanics, technicians, scientists, software engineers, and project managers of the NCAR EOL Research Aviation Facility for their support in the field and in post-processing data. The authors additionally appreciate Martin Schnaiter and Emma Järvinen for providing the PHIPS data.

References

- Abdelmonem, A., Järvinen, E., Duft, D., Hirst, E., Vogt, S., Leisner, T., & Schnaiter, M. (2016). PHIPS-HALO: The airborne Particle Habit Imaging and Polar Scattering probe—Part 1: Design and operation. *Atmospheric Measurement Techniques*, 9, 3131–3144.
- Arabas, S., Pawlowska, H., & Grabowski, W. (2009). Effective radius and droplet spectral width from in-situ aircraft observations in trade-wind cumuli during RICO. *Geophysical Research Letters*, 36(11). <https://doi.org/10.1029/2009gl038257>
- Baumgardner, D., Abel, S. J., Axisa, D., Cotton, R., Crosier, J., Field, P., et al. (2017). Cloud ice properties: In situ measurement challenges. *Meteorological Monographs*, 58, 9–1.
- Baumgardner, D., & Korolev, A. (1997). Airspeed corrections for optical array probe sample volumes. *Journal of Atmospheric and Oceanic Technology*, 14(5), 1224–1229.
- Berg, L. K., Berkowitz, C. M., Barnard, J. C., Senum, G., & Springston, S. R. (2011). Observations of the first aerosol indirect effect in shallow cumuli. *Geophysical Research Letters*, 38(3). <https://doi.org/10.1029/2010gl046047>
- Bodas-Salcedo, A., Hill, P. G., Furtado, K., Williams, K. D., Field, P. R., Manners, J. C., et al. (2016). Large contribution of supercooled liquid clouds to the solar radiation budget of the Southern Ocean. *Journal of Climate*, 29(11), 4213–4228.
- Bony, S., & Dufresne, J. L. (2005). Marine boundary layer clouds at the heart of tropical cloud feedback uncertainties in climate models. *Geophysical Research Letters*, 32(20). <https://doi.org/10.1029/2005gl023851>
- Brenguier, J. L. (1991). Parameterization of the condensation process: A theoretical approach. *Journal of the Atmospheric Sciences*, 48, 264–282.
- Brenguier, J.-L., Bourriane, T., Coelho, A. A., Isbert, J., Peytavi, R., Trevarin, D., & Weschler, P. (1998). Improvements of droplet size distribution measurements with the Fast-FSSP (Forward Scattering Spectrometer Probe). *Journal of Atmospheric and Oceanic Technology*, 15(5), 1077–1090.
- Burnet, F., & Brenguier, J.-L. (2007). Observational study of the entrainment-mixing process in warm convective clouds. *Journal of the Atmospheric Sciences*, 64(6), 1995–2011.
- Cai, Y., Montague, D. C., Mooiweer-Bryan, W., & Deshler, T. (2008). Performance characteristics of the ultra high sensitivity aerosol spectrometer for particles between 55 and 800 nm: Laboratory and field studies. *Journal of Aerosol Science*, 39(9), 759–769.
- Ceppi, P., Zelinka, M. D., & Hartmann, D. L. (2014). The response of the Southern Hemispheric eddy-driven jet to future changes in short-wave radiation in CMIP5. *Geophysical Research Letters*, 41(9), 3244–3250. <https://doi.org/10.1002/2014gl060043>
- Chen, J., Liu, Y., Zhang, M., & Peng, Y. (2016). New understanding and quantification of the regime dependence of aerosol-cloud interaction for studying aerosol indirect effects. *Geophysical Research Letters*, 43(4), 1780–1787. <https://doi.org/10.1002/2016gl067683>
- Chen, J., Liu, Y., Zhang, M., & Peng, Y. (2018). Height dependency of aerosol-cloud interaction regimes. *Journal of Geophysical Research: Atmospheres*, 123(1), 491–506. <https://doi.org/10.1002/2017jd027431>
- Cober, S. G., Isaac, G. A., Korolev, A. V., & Strapp, J. W. (2001). Assessing cloud-phase conditions. *Journal of Applied Meteorology*, 40(11), 1967–1983.
- Cooper, W. A., Friesen, R. B., Hayman, M., Jensen, J., Lenschow, D. H., Romashkin, P., et al. (2016). *Characterization of uncertainty in measurements of wind from the NSF/NCAR Gulfstream V Research Aircraft (No. NCAR/TN-528+STR)*. <https://doi.org/10.5065/D60G3HJ8>
- Desai, N., Glienke, S., Fugal, J., & Shaw, R. A. (2019). Search for microphysical signatures of stochastic condensation in marine boundary layer clouds using airborne digital holography. *Journal of Geophysical Research: Atmospheres*, 124(5), 2739–2752. <https://doi.org/10.1029/2018jd029033>
- Dong, X., Zhao, C., Yang, Y., Wang, Y., Sun, Y., & Fan, R. (2020). Distinct change of supercooled liquid cloud properties by aerosols from an aircraft-based seeding experiment. *Earth and Space Science*, 7, e2020EA001196.
- Earle, M. E., Liu, P. S. K., Strapp, J. W., Zelenyuk, A., Imre, D., McFarquhar, G. M., et al. (2011). Factors influencing the microphysics and radiative properties of liquid-dominated Arctic clouds: Insight from observations of aerosol and clouds during ISDAC. *Journal of Geophysical Research*, 116, D00T09. <https://doi.org/10.1029/2011jd015887>
- Field, P. R., Heymsfield, A. J., & Bansemmer, A. (2006). Shattering and particle interarrival times measured by optical array probes in ice clouds. *Journal of Atmospheric and Oceanic Technology*, 23(10), 1357–1371.
- Garrett, T. J., & Zhao, C. (2006). Increased Arctic cloud longwave emissivity associated with pollution from mid-latitudes. *Nature*, 440, 787–789.
- Haynes, J. M., Jakob, C., Rossow, W. B., Tselioudis, G., & Brown, J. (2011). Major characteristics of Southern Ocean cloud regimes and their effects on the energy budget. *Journal of Climate*, 24(19), 5061–5080.
- Heymsfield, A. J., & McFarquhar, G. M. (2001). Microphysics of INDOEX clean and polluted trade cumulus clouds. *Journal of Geophysical Research*, 106(D22), 28653–28673. <https://doi.org/10.1029/2000jd900776>
- Heymsfield, A. J., & Parrish, J. L. (1978). A computational technique for increasing the effective sampling volume of the PMS two-dimensional particle size spectrometer. *Journal of Applied Meteorology*, 17(10), 1566–1572.
- Holroyd, E. W., III (1987). Some techniques and uses of 2D-C habit classification software for snow particles. *Journal of Atmospheric and Oceanic Technology*, 4(3), 498–511.

- Hu, Y., Winker, D., Vaughan, M., Lin, B., Omar, A., Trepte, C., et al. (2009). CALIPSO/CALIOP cloud phase discrimination algorithm. *Journal of Atmospheric and Oceanic Technology*, *26*(11), 2293–2309.
- Huang, Y., Protat, A., Siems, S. T., & Manton, M. J. (2015). A-Train observations of maritime midlatitude storm-track cloud systems: Comparing the Southern Ocean against the North Atlantic. *Journal of Climate*, *28*(5), 1920–1939.
- Huang, Y., Siems, S. T., Manton, M. J., Hande, L. B., & Haynes, J. M. (2012). The structure of low-altitude clouds over the Southern Ocean as seen by CloudSat. *Journal of Climate*, *25*(7), 2535–2546.
- Hudson, J. G., & Yum, S. S. (1997). Droplet spectral broadening in marine stratus. *Journal of the Atmospheric Sciences*, *54*(22), 2642–2654.
- Khain, A., Ovtchinnikov, M., Pinsky, M., Pokrovsky, A., & Krugliak, H. (2000). Notes on the state-of-the-art numerical modeling of cloud microphysics. *Atmospheric Research*, *55*(3–4), 159–224.
- Khain, A., Prabha, T. V., Benmoshe, N., Pandithurai, G., & Ovchinnikov, M. (2013). The mechanism of first raindrops formation in deep convective clouds. *Journal of Geophysical Research: Atmospheres*, *118*(16), 9123–9140. <https://doi.org/10.1002/jgrd.50641>
- King, W. D., Dye, J. E., Baumgardner, D., Strapp, J. W., & Huffman, D. (1985). Icing wind tunnel tests on the CSIRO liquid water probe. *Journal of Atmospheric and Oceanic Technology*, *2*(3), 340–352.
- King, W. D., Parkin, D. A., & Handsworth, R. J. (1978). A hot-wire liquid water device having fully calculable response characteristics. *Journal of Applied Meteorology*, *17*(12), 1809–1813.
- Koren, I., Kaufman, Y. J., Rosenfeld, D., Remer, L. A., & Rudich, Y. (2005). Aerosol invigoration and restructuring of Atlantic convective clouds. *Geophysical Research Letters*, *32*(14). <https://doi.org/10.1029/2005gl023187>
- Korolev, A. (2007). Reconstruction of the sizes of spherical particles from their shadow images. Part I: Theoretical considerations. *Journal of Atmospheric and Oceanic Technology*, *24*(3), 376–389.
- Kupc, A., Williamson, C., Wagner, N. L., Richardson, M., & Brock, C. A. (2018). Modification, calibration, and performance of the Ultra-High Sensitivity Aerosol Spectrometer for particle size distribution and volatility measurements during the Atmospheric Tomography Mission (ATom) airborne campaign. *Atmospheric Measurement Techniques*, *11*, 369–383.
- Liu, Y., & Daum, P. H. (2002). Anthropogenic aerosols: Indirect warming effect from dispersion forcing. *Nature*, *419*(6907), 580.
- Liu, Y., Daum, P. H., & Yum, S. S. (2006). Analytical expression for the relative dispersion of the cloud droplet size distribution. *Geophysical Research Letters*, *33*(2). <https://doi.org/10.1029/2005gl024052>
- Lu, C., Liu, Y., Niu, S., & Vogelmann, A. M. (2012). Observed impacts of vertical velocity on cloud microphysics and implications for aerosol indirect effects. *Geophysical Research Letters*, *39*(21). <https://doi.org/10.1029/2012gl053599>
- Lu, C., Liu, Y., Yum, S. S., Chen, J., Zhu, L., Gao, S., et al. (2020). Reconciling contrasting relationships between relative dispersion and volume-mean radius of cloud droplet size distributions. *Journal of Geophysical Research: Atmospheres*, *125*(9), e2019JD031868. <https://doi.org/10.1029/2019jd031868>
- Lu, M. L., Feingold, G., Jonsson, H. H., Chuang, P. Y., Gates, H., Flagan, R. C., & Seinfeld, J. H. (2008). Aerosol-cloud relationships in continental shallow cumulus. *Journal of Geophysical Research*, *113*(D15). <https://doi.org/10.1029/2007jd009354>
- Lu, M. L., & Seinfeld, J. H. (2006). Effect of aerosol number concentration on cloud droplet dispersion: A large-eddy simulation study and implications for aerosol indirect forcing. *Journal of Geophysical Research*, *111*(D2). <https://doi.org/10.1029/2005jd006419>
- Magaritz-Ronen, L., Khain, A., & Pinsky, M. (2016). About the horizontal variability of effective radius in stratocumulus clouds. *Journal of Geophysical Research: Atmospheres*, *121*(16), 9640–9660. <https://doi.org/10.1002/2016JD024977>
- Martin, G. M., Johnson, D. W., & Spice, A. (1994). The measurement and parameterization of effective radius of droplets in warm stratocumulus clouds. *Journal of the Atmospheric Sciences*, *51*(13), 1823–1842.
- McFarlane, S. A., & Grabowski, W. W. (2007). Optical properties of shallow tropical cumuli derived from ARM ground-based remote sensing. *Geophysical Research Letters*, *34*(6). <https://doi.org/10.1029/2006gl028767>
- McFarquhar, G. M., Baumgardner, D., Bansemir, A., Abel, S. J., Crosier, J., French, J., et al. (2017). Processing of ice cloud in situ data collected by bulk water, scattering and imaging probes: Fundamentals, uncertainties and efforts towards consistency. *American Meteorological Society*, *58*(II), 11.1–11.33.
- McFarquhar, G. M., Bretherton, C., Marchand, R., Protat, A., DeMott, P., Alexander, S., et al. (2021). Unique observations of clouds, aerosols and precipitation over the Southern Ocean: An overview of CAPRICORN, MARCUS, MICRE and SOCRATES. *Bulletin of the American Meteorological Society*, 1–92.
- McFarquhar, G. M., Finlon, J. A., Stechman, D. M., Wu, W., Jackson, R. C., & Freer, M. (2018). *University of Illinois/Oklahoma optical array probe (OAP) processing software*. <https://doi.org/10.5281/zenodo.1285969>
- McFarquhar, G. M., & Heymsfield, A. J. (2001). Parameterizations of INDOEX microphysical measurements and calculations of cloud susceptibility: Applications for climate studies. *Journal of Geophysical Research*, *106*(D22), 28675–28698.
- McFarquhar, G. M., Timlin, M. S., Rauber, R. M., Jewett, B. F., Grim, J. A., & Jorgensen, D. P. (2007). Vertical variability of cloud hydrometeor in the stratiform region of mesoscale convective systems and bow echoes. *Monthly Weather Review*, *135*, 3405–3428.
- McFarquhar, G. M., Zhang, G., Poellot, M. R., Kok, G. L., McCoy, R., Tooman, T., et al. (2007). Ice properties of single-layer stratocumulus during the Mixed-Phase Arctic Cloud Experiment: 1. Observations. *Journal of Geophysical Research*, *112*, D24201. <https://doi.org/10.1029/2007jd008633>
- Miles, N. L., Verlinde, J., & Clothiaux, E. E. (2000). Cloud droplet size distributions in low-level stratiform clouds. *Journal of the Atmospheric Sciences*, *57*(2), 295–311.
- Naud, C. M., Booth, J. F., & Del Genio, A. D. (2014). Evaluation of ERA-Interim and MERRA cloudiness in the Southern Ocean. *Journal of Climate*, *27*(5), 2109–2124.
- Paluch, I. R., & Knight, C. A. (1984). Mixing and the evolution of cloud droplet size spectra in a vigorous continental cumulus. *Journal of the Atmospheric Sciences*, *41*(11), 1801–1815.
- Pawlowska, H., Brenguier, J. L., & Burnet, F. (2000). Microphysical properties of stratocumulus clouds. *Atmospheric Research*, *55*(1), 15–33.
- Pawlowska, H., Grabowski, W. W., & Brenguier, J. L. (2006). Observations of the width of cloud droplet spectra in stratocumulus. *Geophysical Research Letters*, *33*(19). <https://doi.org/10.1029/2006gl026841>
- Peng, Y., & Lohmann, U. (2003). Sensitivity study of the spectral dispersion of the cloud droplet size distribution on the indirect aerosol effect. *Geophysical Research Letters*, *30*(10). <https://doi.org/10.1029/2003gl017192>
- Peng, Y., Lohmann, U., Leitch, R., & Kulmala, M. (2007). An investigation into the aerosol dispersion effect through the activation process in marine stratus clouds. *Journal of Geophysical Research*, *112*, D11117. <https://doi.org/10.1029/2006jd007401>
- Pinsky, M., Mazin, I. P., Korolev, A., & Khain, A. (2014). Supersaturation and diffusional droplet growth in liquid clouds: Polydisperse spectra. *Journal of Geophysical Research: Atmospheres*, *119*(22), 12–872. <https://doi.org/10.1002/2014jd021885>
- Politovich, M. K. (1993). A study of the broadening of droplet size distributions in cumuli. *Journal of the Atmospheric Sciences*, *50*(14), 2230–2244.

- Schnaiter, M. (2018). *PHIPS-HALO stereo imaging data. Version 1.0 (version 1.0) [data set]*. UCAR/NCAR—Earth Observing Laboratory. <https://doi.org/10.5065/d62b8wwf>
- Schnaiter, M., Järvinen, E., Abdelmonem, A., & Leisner, T. (2018). PHIPS-HALO: The airborne particle habit imaging and polar scattering probe—Part 2: Characterization and first results. *Atmospheric Measurement Techniques*, *11*(1), 341.
- Seinfeld, J. H., Bretherton, C., Carslaw, K. S., Coe, H., DeMott, P. J., Dunlea, E. J., et al. (2016). Improving our fundamental understanding of the role of aerosol–cloud interactions in the climate system. *Proceedings of the National Academy of Sciences of the United States of America*, *113*(21), 5781–5790.
- Sinclair, K., van Dienenhoven, B., Cairns, B., Alexandrov, M., Moore, R., Ziemba, L. D., & Crosbie, E. (2020). Observations of aerosol–cloud interactions during the North Atlantic aerosol and marine ecosystem study. *Geophysical Research Letters*, *47*, e2019GL085851. <https://doi.org/10.1029/2019gl085851>
- Slingo, A., & Schrecker, H. M. (1982). On the shortwave radiative properties of stratiform water clouds. *Quarterly Journal of the Royal Meteorological Society*, *108*(456), 407–426.
- Stephens, G. L. (1978). Radiation profiles in extended water clouds. I: Theory. *Journal of the Atmospheric Sciences*, *35*(11), 2111–2122.
- Stephens, G. L., & Platt, C. M. R. (1987). Aircraft observations of the radiative and microphysical properties of stratocumulus and cumulus cloud fields. *Journal of Climate and Applied Meteorology*, *26*(9), 1243–1269.
- Trenberth, K. E., & Fasullo, J. T. (2010). Simulation of present-day and twenty-first-century energy budgets of the southern oceans. *Journal of Climate*, *23*(2), 440–454.
- UCAR/NCAR—Earth Observing Laboratory. (2018). *NCAR HSRL lidar data. Version 1.0 [data set]*. UCAR/NCAR—Earth Observing Laboratory. <https://doi.org/10.5065/d6pk0f1t>
- Wang, J., Daum, P. H., Yum, S. S., Liu, Y., Senum, G. I., Lu, M. L., et al. (2009). Observations of marine stratocumulus microphysics and implications for processes controlling droplet spectra: Results from the Marine Stratus/Stratocumulus Experiment. *Journal of Geophysical Research*, *114*(D18). <https://doi.org/10.1029/2008jd011035>
- Wang, Y., McFarquhar, G. M., Rauber, R. M., Zhao, C., Wu, W., Finlon, J. A., et al. (2020). Microphysical properties of generating cells over the Southern Ocean: Results from SOCRATES. *Journal of Geophysical Research: Atmospheres*, *125*(13), e2019JD032237. <https://doi.org/10.1029/2019jd032237>
- Wang, Z., Letu, H., Shang, H., Zhao, C., Li, J., & Ma, R. (2019). A supercooled water cloud detection algorithm using Himawari-8 satellite measurements. *Journal of Geophysical Research: Atmospheres*, *124*, 2724–2738. <https://doi.org/10.1029/2018jd029784>
- Warner, J. (1969). The microstructure of cumulus cloud. Part I. General features of the droplet spectrum. *Journal of the Atmospheric Sciences*, *26*(5), 1049–1059.
- Warner, J. (1973). The microstructure of cumulus cloud: Part IV. The effect on the droplet spectrum of mixing between cloud and environment. *Journal of the Atmospheric Sciences*, *30*(2), 256–261.
- Wood, R. (2012). Stratocumulus clouds. *Monthly Weather Review*, *140*(8), 2373–2423.
- Wu, W., & McFarquhar, G. M. (2016). On the practical definitions of maximum dimension for non-spherical particles recorded by 2D probes. *Journal of Atmospheric and Oceanic Technology*, *33*, 1057–1072.
- Wu, W., & McFarquhar, G. M. (2019). *NSF/NCAR G-V HIAPER 2D-S particle size distribution (PSD) product data [data set]. Version 1.1*. UCAR/NCAR—Earth Observing Laboratory. <https://doi.org/10.26023/8HMG-WQP3-XA0X>
- Wyant, M. C., Bretherton, C. S., Rand, H. A., & Stevens, D. E. (1997). Numerical simulations and a conceptual model of the stratocumulus to trade cumulus transition. *Journal of the Atmospheric Sciences*, *54*(1), 168–192.
- Yang, F., Kollias, P., Shaw, R. A., & Vogelmann, A. M. (2018). Cloud droplet size distribution broadening during diffusional growth: Ripening amplified by deactivation and reactivation. *Atmospheric Chemistry and Physics*, *18*(10), 7313–7328.
- Yang, Y., Zhao, C., Dong, X., Fan, G., Zhou, Y., Wang, Y., et al. (2019). Toward understanding the process-level impacts of aerosols on microphysical properties of shallow cumulus cloud using aircraft observations. *Atmospheric Research*, *221*, 27–33.
- Yeom, J. M., Yum, S. S., Mei, F., Schmid, B., Comstock, J., Machado, L. A. T., & Cecchini, M. A. (2019). Impact of secondary droplet activation on the contrasting cloud microphysical relationships during the wet and dry seasons in the Amazon. *Atmospheric Research*, *230*, 104648.
- Yum, S. S., & Hudson, J. G. (2005). Adiabatic predictions and observations of cloud droplet spectral broadness. *Atmospheric Research*, *73*(3–4), 203–223.
- Zhao, C., Qiu, Y., Dong, X., Wang, Z., Peng, Y., Li, B., et al. (2018). Negative aerosol–cloud relationship from aircraft observations over Hebei, China. *Earth and Space Science*, *5*(1), 19–29.
- Zhao, C., Tie, X., Brasseur, G., Noone, K. J., Nakajima, T., Zhang, Q., et al. (2006). Aircraft measurements of cloud droplet spectral dispersion and implications for indirect aerosol radiative forcing. *Geophysical Research Letters*, *33*(16). <https://doi.org/10.1029/2006gl026653>
- Zhao, C., Xie, S., Klein, S. A., Protat, A., Shupe, M. D., McFarlane, S. A., et al. (2012). Toward understanding of differences in current cloud retrievals of ARM ground-based measurements. *Journal of Geophysical Research*, *117*, D10206. <https://doi.org/10.1029/2011jd016792>
- Zhao, C., Zhao, L., & Dong, X. (2019). A case study of stratus cloud properties using in situ aircraft observations over Huanghua, China. *Atmosphere*, *10*(1), 19.